Hybrid high-performance aqueous batteries with potassium-based cathode||zinc metal anode

Weijian Yu[1†], Junmin Ge[1†], Yanyao Hu[1], Dongyang Shen[1], Wendi Luo[1], Suhua Chen[2], Lichen Wu[1], Zhaomeng Liu[3], Jiang Zhou[4], Hongguan Yang[1*] and Bingan Lu[1,5*]

ABSTRACT Aqueous potassium-based batteries (APBs) have been widely studied for their high safety and environmentally friendly properties. However, given the limitation of the electrode material and working mechanism, the APBs need further improvement in terms of the rate performance and energy density to meet the development requirements. To address the above issues, we successfully designed and assembled APBs, for the first time using Zn metal as the anode, $K_{1.92}Cu_{0.62}Mn_{0.38}[Fe(CN)_6]_{0.968} \cdot \square_{0.032} \cdot 0.35H_2O$ as the cathode, and $2\ mol\ L^{-1}\ Zn(SO_3CF_3)_2 + 12\ mol\ L^{-1}\ KSO_3CF_3$ as the electrolyte. This hybrid-ion-battery (HIB) design offers benefits including the following: (i) improvement of the working potential of APBs by selecting Zn metal as the anode, (ii) shortened ion transport path due to the dual-cation storage mechanism, and (iii) inhibition of the growth of zinc dendrite through the electrostatic shielding effect enabled by K^+, which originated from the dual-cation electrolyte. As a result, the as-assembled full battery had a high working potential of 1.75 V and excellent rate performance (83.3% of original capacity was maintained at the current density of $10,000\ mA\ g^{-1}$). Furthermore, the *in-situ* electrostatic shielding effect, which can significantly inhibit the dendrite growth of the Zn anode and improve the stability of the full battery, was fully revealed by theoretical phase-field simulation and comprehensive characterizations. The fascinating structure design of HIBs sheds light on the development of high-performance APBs.

Keywords: aqueous potassium-based batteries, Prussian blue analogues, hybrid-ion batteries, high-rate, electrostatic shielding effect

INTRODUCTION

The limitations of renewable energies, such as the unpredictable availability and non-uniformity in distribution, urge the development of large-scale energy storage systems [1–12]. Among many energy storage technologies, a rechargeable battery based on the conversion between electric and chemical energy is one of the most effective methods due to its unparalleled conversion efficiency. Owing to their high safety and environmentally friendly properties, aqueous metal ion (such as Li^+, Na^+, K^+, and Zn^{2+}) batteries (AMIBs) have gained considerable attention [13–19]. Among various AMIBs, aqueous potassium-based batteries (APBs) are highly promising due to their low cost and small Stocks radius, matching the requirements of large-scale storage, such as cheap and easy establishment and applicability in high-rate charge/discharge circumstances [20–22]. However, the energy density and stability of reported APBs are still less satisfying as they usually exploit organic anode materials, such as perylene-3,4,9,10-tetracarbox-diimide (PTCDI) or perylene-3,4,9,10-tetracarboxylic dianhydride (PTCDA), both of which coordinate/de-coordinate potassium ions at a high voltage, leading to low working potential and unsatisfying energy density for APBs [23–29].

Another factor that determines the output voltage of APBs is the working potential of the cathode material. To date, the reported high-potential cathode materials of potassium-ion batteries can be classified into three categories: transitional metal oxides [30], polyanionic materials [31], and Prussian blue analogs (PBAs) [32]. Given their good hydrophilicity, facile synthesis, low cost, and high operating potential, PBAs have also been extensively used as cathodes in APBs. Among various PBAs, potassium manganese ferrocyanide (MnPB) exhibits the highest reversible capacity and working potential because both Mn and Fe ions in the crystal are electrochemically active in storing potassium ions at a high voltage. However, given the Jahn-Teller effect, which occurs when Mn^{2+} is oxidized to Mn^{3+}, the capacity of pure MnPB decreases rapidly. Lattice instability leads to the disproportionation and dissolution of Mn^{3+}, resulting in the cyclic instability of many Mn-containing compounds [33]. Several groups have reported their methods for solving this problem. For example, Ge *et al.* [1] realized the ultra-long stable cycle of MnPB through a surface substitution method. Moreover, Li *et al.* [34] inhibited the capacity decay of MnPB by coating with conductive polymers. However, these methods are usually costly and difficult to control, making them extremely cumbersome in practical applications. Previous studies have

[1] School of Physics and Electronics, Hunan University, Changsha 410082, China
[2] School of Physics and Electronics, Henan University, Kaifeng 475004, China
[3] School of Metallurgy, Northeastern University, Shenyang 110819, China
[4] School of Materials Science and Engineering, Key Laboratory of Electronic Packaging and Advanced Functional Materials of Hunan province, Central South University, Changsha 410083, China
[5] State Key Laboratory of Advanced and Manufacturing for Vehicle Body, Hunan University, Changsha 410082, China
[†] These authors contributed equally to this work.
[*] Corresponding authors (emails: yanghg@hnu.edu.cn (Yang H); luba2012@hnu.edu.cn (Lu B))

shown that copper ferrocyanide (CuPB) can provide an extremely stable cycle performance, and MnPB and CuPB share a similar lattice structure, which means that Cu ions should be easily doped into the crystal structure of MnPB without causing its distortion or collapse [35]. This structural design may improve the cycle performance of MnPB by restraining the Jahn-Teller effect and the dissolution of Mn^{3+} ions.

Rate performance is one of the essential configurations for APBs to evaluate their potential for practical application. The optimization of the rate performance of APBs usually lies in the modification of the conductivity of electrode materials [2] and the ion transfer rate of electrolytes [23]; however, studies on the improvement of their ion transfer mechanism are limited. In this study, we developed a partially copper-substituted potassium manganese ferrocyanide (KCM) cathode by a one-step synthesis strategy and applied it to a potassium-zinc hybrid-ion battery (PZ-HIB) to establish stable and high-output-voltage AMIBs for the first time. The as-prepared PZ-HIB delivered a high output voltage of 1.75 V and can maintain 77.6% of its original capacity over 1400 cycles. It can also provide excellent rate performance (the capacity remained at 83.6% at the current density of 10,000 mA g^{-1}). Furthermore, the potassium ions in the hybrid-ion electrolyte (HIE) can effectively inhibit the dendrite growth on the zinc anode side.

EXPERIMENTAL SECTION

Synthesis of $K_xCu_yMn_{1-y}[Fe(CN)_6]$
In a 300-mL round-bottomed flask, copper chloride hexahydrate ($CuCl_2 \cdot 6H_2O$; 0.341 g, 2 mmol), manganese acetate tetrahydrate ($Mn(CH_3COO)_2 \cdot 4H_2O$; 0.24509 g, 1 mmol), and potassium citrate (4 g) were dissolved in 100 mL deionized water and stirred for 30 min to obtain solution A. $K_4Fe(CN)_6 \cdot 10H_2O$ (1.79 g, 4.25 mmol) was dissolved in 100 mL deionized water to obtain solution B. The reaction rate was controlled by a separation funnel, and solution A was slowly added to solution B (drop addition rate: 6 drops per minute) with stirring. The reaction solution was stirred at room temperature for 24 h and then aged for another 24 h. The obtained mixed solution was centrifuged and repeatedly washed with deionized water and ethanol. $K_xCu_yMn_{1-y}[Fe(CN)_6]$ was dried overnight in a vacuum oven at 80°C. Based on the ratio of copper to manganese in the synthesis process, the samples were denoted as KCM-21, KCM-11, and KCM-12.

Preparation of electrodes and electrolyte
The positive electrode was made of a slurry consisting of 70% active material, 20% Ketjen black, and 10% polyvinylidene fluoride binder. N-methyl-2-pyrrolidone was used as a dispersant. Then, the paste was coated on the titanium mesh (1 cm^2) and dried overnight at 80°C with a active material loading of 1.25 mg cm^{-1}. As negative electrodes, zinc sheets (1 cm^2) were rinsed and polished with alcohol. The electrolytes used comprised 2 mol L^{-1} zinc trifluoromethanesulfonate ($Zn[OTf]_2$, 98% wt%) and 12 mol L^{-1} potassium trifluoromethanesulfonate (KOTf, 98% wt%), both of which were dissolved in ultrapure water.

Material characterization
Scanning electron microscopy (SEM, TESCAN MIRA4 LMH) and transmission electron microscopy (TEM, JEM-2100F) were used to observe the morphology and microstructure of the samples. The corresponding energy dispersive spectroscopy (EDS, One Max 50) was also performed. Powder X-ray diffraction (XRD) data were collected by a Bruker D8 Advanced diffractometer (Cu Kα radiation). The elemental valence states were tested by X-ray photoelectron spectroscopy (XPS, Thermo Scientific K-Alpha). The 20-nm argon-ion sputtering process helped remove the possible surface contamination on the characterized surfaces. Inductively coupled plasma (ICP) tests were conducted on an Agilent ICPMS7800. Thermogravimetric analysis (TGA) characterization was conducted using Pyris diamond thermogravimetric/differential thermal analysis (HCT-1) under a N_2 atmosphere at a heating rate of 5°C min^{-1}. The vibration states of functional groups were examined via Fourier transform infrared spectrophotometry (FT-IR, AVTATAR, 370) in the frequency range from 500 to 4000 cm^{-1} with KBr as a reference. The retrieved electrodes for the SEM characterizations were obtained by disassembling the batteries at room temperature, where they were washed with ultrapure water to remove the residual electrolyte salts. A conductivity meter (DDSJ-307F) was used to test the ionic conductivity of the K-Zn dual-cation electrolyte.

Electrochemical measurements
To carry out the electrochemical test, we assembled 2032 coin cells in an air environment at room temperature using zinc metal as the counter electrode and a glass microfiber filter (Whatman, Grade GF/D) as the separator. Galvanostatic charge/discharge test results were recorded at 25°C with a Land battery testing system (LAND, China). The specific capacity was calculated from the mass of the active substance. The battery's cyclic voltammetry (CV) curves and electrochemical impedance spectroscopy were measured using a potentiostat/galvanostat (CHI 760D) within the range of 10^{-2}–10^5 Hz, and the initial voltage of measurement was set to the open-circuit voltage of the battery.

Phase-field simulation
All the simulations in this work were performed by COMSOL Multiphysics 5.6 with an implemented finite element solver. The phase-field simulations of the Zn plating morphological evolution were conducted in a 25 μm × 25 μm cell electrodeposition system. The diffusion coefficient of zinc ions was set as 1.8×10^{-9} m^2 S^{-1}, and the concentration was set to 10 mol m^{-3}.

RESULTS AND DISCUSSION
As shown in Fig. 1a, the redox potentials of the anode and cathode together determine the operating voltage of batteries. PBAs have been widely studied as positive electrodes due to their ideal redox potential (MnPB, i.e., the potassium-ion embedding potential is approximately 0.99 V vs. H/H^+) and excellent hydrophilicity. When matching APBs, anodes with negative potassium-ion embedding potentials are required, with PTCDI (i.e., −0.49 V vs. H/H^+) and PTCDA (i.e., −0.49 V vs. H/H^+) usually being selected [1,36]. Compared with these compounds, zinc has the lowest redox potential (−0.76 V vs. H/H^+). Combining a reasonable design, PZ-HIB will have a wider working potential range theoretically. Fig. 1b shows the working mechanism of the assembled PZ-HIB. As the thermodynamic redox potential of Zn/Zn^{2+} is 2.169 V higher than that of K/K^+, the deposition/dissolution of Zn^{2+} ions at the anode side should
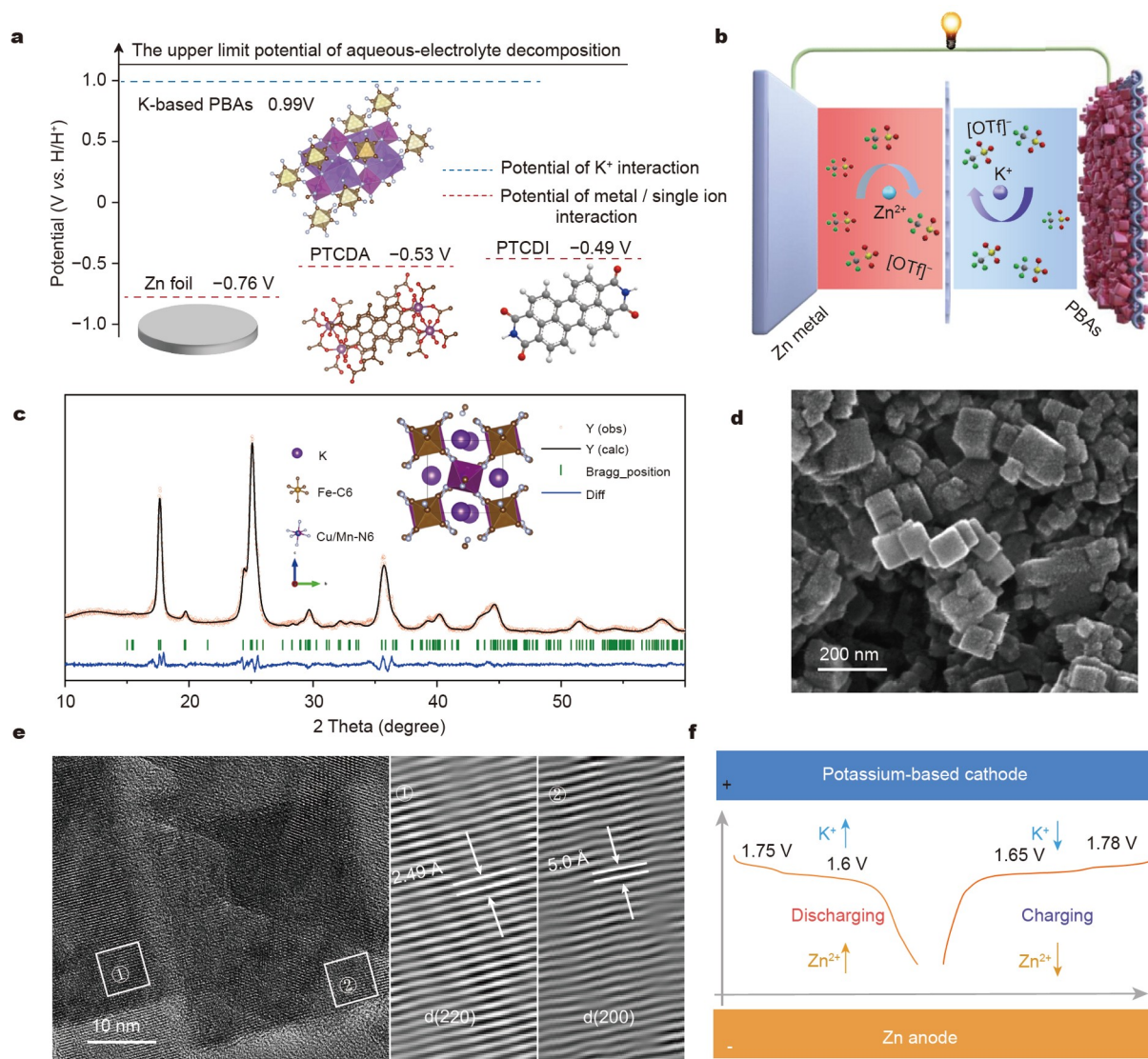
Figure 1 Design concept and improved operated potential of KCM-21. (a) Voltage window of different anodes matched with the Prussian blue cathode in aqueous batteries. (b) Schematic of the working mechanism of as-prepared PZ-HIB. (c) Rietveld refinement XRD pattern. The inset is the crystal structure of KCM-21. (d) SEM image, (e) TEM image and HRTEM images of KCM-21. (f) Schematic illustration of improved potential curves by K^+ and Zn^{2+} ions.

be preferred compared with K^+ ions. The interaction reaction on the cathode side is dominated by K^+ because Zn^{2+} has a higher valence state, and the diffusion rate is several orders of magnitude slower than that of K^+ in the same substrate [37]. The working mechanism of this PZ-HIB can be summarized as follows. During the charging process, the potassium ions that are pre-stored in the cathode are de-intercalated from the material and transferred into the electrolyte, and zinc ions in the electrolyte receive electrons on the surface of the zinc foil and plate. Meanwhile, during the discharging procedure, the reversible process occurs. In addition, the battery voltage needs to be within the electrochemical stability window of the electrolyte solution to eliminate the O_2 and H_2 produced by hydrolysis. In practice, kinetic effects, including the overpotential of H_2/O_2 on the electrode surface and the interaction between ions and solvents, increase the difficulty of water decomposition. The voltage window can be raised to 2 V with a high concentration of aqueous electrolyte [38]. Coin cells were tested on a laboratory scale with 2 mol L^{-1} $Zn(SO_3CF_3)_2$ + 12 mol L^{-1} KSO_3CF_3 aqu-

eous solution as the electrolyte (Fig. S1).

PBAs have a three-dimensional open and flexible skeleton, which is beneficial for the reversible storage of large ions, such as K^+. Furthermore, they can be hardly soluble in aqueous systems and usually provide a high working potential, making them suitable as cathode materials for AMIBs. Fig. S2 shows a typical synthesis route for KCM. Usually, during the co-precipitation process, the reaction rate in the aqueous solution is extremely too fast to control. Therefore, H_2O molecules will inevitably participate in the precipitation process and become capsuled into the PBAs' crystal structure, which is adverse to their electrochemical stability. To solve this problem, scientists added a chelating agent to slow down the precipitation rate of $K_xCu_yMn_{1-y}[Fe(CN)_6]$ [39]. To explore the stabilizing effect of Cu on $K_2Mn[Fe(CN)_6]$, we synthesized a series of $K_xCu_yMn_{1-y}$-$[Fe(CN)_6]$ with different Cu to Mn ratios (atom ratio) of 1:2, 1:1, and 2:1 (denoted as KCM-12, KCM-11, and KCM-21, respectively). Here we focused on the analysis of the KCM-21 sample. The structure of KCM-21 was identified by powder XRD and

Rietveld refinement (Fig. 1c). The test results showed that KCM-21 had a monoclinic phase ($P21/C$ space group, $a = 6.9853$ Å, $b = 7.29950$ Å, $c = 12.171$ Å, and $\alpha = \gamma = 90°$). The placeholder information for each atom is listed in Table S1. Moreover, as shown by the inset of Fig. 1c, KCM-21 exhibited an open-skeleton structure, in which each Fe and Mn/Cu ion coordinated with six C and N atoms, respectively. According to the test results of SEM, KCM-21 was made of regular and aggregated cubes with a nanometer diameter of 30–40 nm (Fig. 1d). These nanocubes effectively decreased the transport distance of potassium ions in the KCM-21 crystal and facilitated the infiltration of electrolytes. As displayed in the high-resolution TEM (HRTEM) images (Fig. 1e), the lattice fringes of the as-prepared material in the direction of conduction 200 and 220 ($d_{200} = 5.0$ Å and $d_{220} = 2.49$ Å, respectively) can be observed and corresponded well with the XRD results. EDS element mappings (Fig. S3) proved the existence of Fe, Cu, and Mn, all of which were evenly distributed across all cubes. ICP-mass spectrometry (ICP-MS) was utilized to determine the specific content of each element. As shown in Table S2, the molar ratio of K:Mn:Cu:Fe was 1.92:0.38:0.62:0.968, indicating its high K^+ ion content and almost zero $[Fe(CN)_6]$ vacancy (3.2 at% vs. Mn/Cu). TGA was also used to estimate the water content in the as-prepared KCM-21. As shown in Fig. S4, approximately 1.1 wt% moisture in KCM-21 evaporated from room temperature to 117°C, and from 117 to 213°C, the weight loss was 2.3 wt%, indicating that a small amount of weakly coordinated water molecules existed in KCM-21. Based on the ICP-MS and TGA results, the chemical formula of KCM-21 is $K_{1.92}Cu_{0.62}Mn_{0.38}[Fe(CN)_6]_{0.968} \cdot \square_{0.032} \cdot 0.35H_2O$, which is close to its theoretical formula: $K_2Cu_{0.67}Mn_{0.33}[Fe(CN)_6]$. Moreover, the FT-IR spectrum of KCM-21 showed one strong and two weak peaks centered at 2076, 3424 and 1641 cm^{-1}, respectively, corresponding to the existence of $Mn^{2+}–N\equiv C–Fe^{2+}$ bonds and water molecules (Fig. S5), which matched well the ICP-MS and TGA results. XPS was also employed to observe the surface composition of KCM-21 and investigate the valence states of Fe, Mn, and Cu (Fig. S6a). In the Fe 2p spectrum, the adsorption bands located at 708.35 and 721.10 eV in the spectrum were associated with Fe^{II} $2p_{3/2}$ and Fe^{III} $2p_{1/2}$, respectively. Another peak for Fe^{III} at 716.63 eV appeared, and it indicated the existence of KCM-21 (Fig. S6b). In the Cu 2p spectrum, the absorption bands located at 933.21 and 953.22 eV corresponded to Cu^{II} $2p_{1/2}$ and Cu^{II} $2p_{3/2}$, respectively (Fig. S6c). Furthermore, in the Mn 2p spectrum, two peaks located at 641.60 and 644.10 eV appeared, and they corresponded to Mn^{II} and Mn^{III}, respectively, confirming the coexistence of Mn^{II} and Mn^{III} in the KCM-21 sample [40,41] (Fig. S6d).

Characterizations of $K_xCu_yMn_{1-y}[Fe(CN)_6]$

The thermodynamics and kinetics of K^+ were studied by galvanostatic intermittent titration technique (GITT). The capacity of the first charge measured by GITT was higher than that of the constant current process (Fig. S7a). This finding was due to the relaxation process between pulsed currents during the charge/discharge process. Fig. S7b presents a typical single-step titration at around 1.7 V, which was measured with a pulse current at 10,000 mA g^{-1} for 30 s and relaxed at the open circuit for 600 s to reach the quasi-equilibrium. As shown in Fig. S7c, $dE/d\sqrt{t}$ shows the expected straight line behavior, the chemical diffusion coefficient D_k can be estimated from Fick's second law (Sup-

plementary information). The calculated chemical diffusion coefficient of K^+ in KCM-21 was around 10^{-9} cm^2 s^{-1} (Fig. S7d). A high value is conducive to rate performance improvement [30].

Given the chelating agent citrate, the defect and crystal water ratio of KCM-21 was low. This result was close to the theoretical stoichiometric ratio of $K_2Cu_{0.67}Mn_{0.33}[Fe(CN)_6]$. Furthermore, high K content and small nanoparticle size had advantages in improving the initial Coulombic efficiency (ICE) and conductivity. To obtain the stability of copper and the high capacity of manganese, we adjusted the ratio of Cu and Mn to 1:2, 1:1, and 2:1 during the synthesis of KCM. SEM was used to observe the morphology of the three samples (Fig. S8a, b). KCM-11 and KCM-12 existed in the form of small nanoparticle stacks with a length of ~30 nm, irregular shapes, and partial agglomeration. The electrochemical performance test of KCM will be discussed in the next section.

Electrochemical performance of HIBs

For APBs, assembling a full battery with high energy density is always a challenge. As shown in Fig. 1f, we paired the high-potential KCM-21||zinc-metal full battery to establish a high-working-voltage (1.75 V vs. Zn/Zn^{2+}) PZ-HIB for the first time.

An HIE, i.e., 2 mol L^{-1} trifluoromethane sulfonic acid zinc salt + 12 mol L^{-1} trifluoromethane sulfonic acid potassium salt aqueous solution, with maximum solubility, was used in this work to conduct potassium and zinc ions. Before the evaluation of the electrochemical performance of this PZ-HIB, a linear scanning voltammetry test of the HIE was carried out to check its stability. As shown in Fig. S9, the oxidation limit of the HIE was around 1.7 V (vs. Zn^{2+}/Zn). When the voltage rose to 2 V, the decomposition current was still small (0.08 mA cm^{-2}). Fig. 2a shows the charge/discharge curves of the as-assembled PZ-HIB at the current density of 2000 mA g^{-1}. During the charging process, two distinct plateaus at 1.65 and 1.78 V were observed. Reversibly, the corresponding two plateaus at 1.75 and 1.60 V can be observed during the subsequent discharging process.

The two redox couples at 1.78/1.75 and 1.65/1.60 V were related to the redox process of Mn^{2+}/Mn^{3+} and Fe^{2+}/Fe^{3+}, respectively. Notably, at the high current density of 2000 mA g^{-1}, the voltage polarization of this PZ-HIB was negligible. The two redox plateaus showed small voltage lags of 30 and 50 μV. In the following 100 cycles, the discharge specific capacity decreased slowly from 113.1 to 103.0 mA h g^{-1}. The voltage generated by the high-spin Mn^{2+}/Mn^{3+} redox pair had no attenuation, indicating that Mn^{2+} dissolution was inhibited. In terms of the electrochemical capacity, KCM was in the middle of CuPB and MnPB, and the capacity from Mn^{2+}/Mn^{3+} voltage was lower than that from Fe^{2+}/Fe^{3+}. The specific capacity depended on the proportion of Mn^{2+}, which was consistent with the predicted results. Fig. S10 shows the curve of the initial charge/discharge initial charging process. PZ-HIB provided a specific capacity of 113.3 mA h g^{-1} in the first discharge process, and this result was close to its theoretical value (~115 mA h g^{-1}). CV measurement showed that at the scanning rate of 0.2 mV s^{-1}, two pairs of redox peaks, which can be assigned to be the redox procedure of Mn^{2+}/Mn^{3+} and Fe^{2+}/Fe^{3+}, can be observed (Fig. S11a), corresponding well with the galvanostatic charge-discharge test results. A pair of small redox peaks appeared at 0.37/1.08 V in the CV test, and it was caused by the deposition
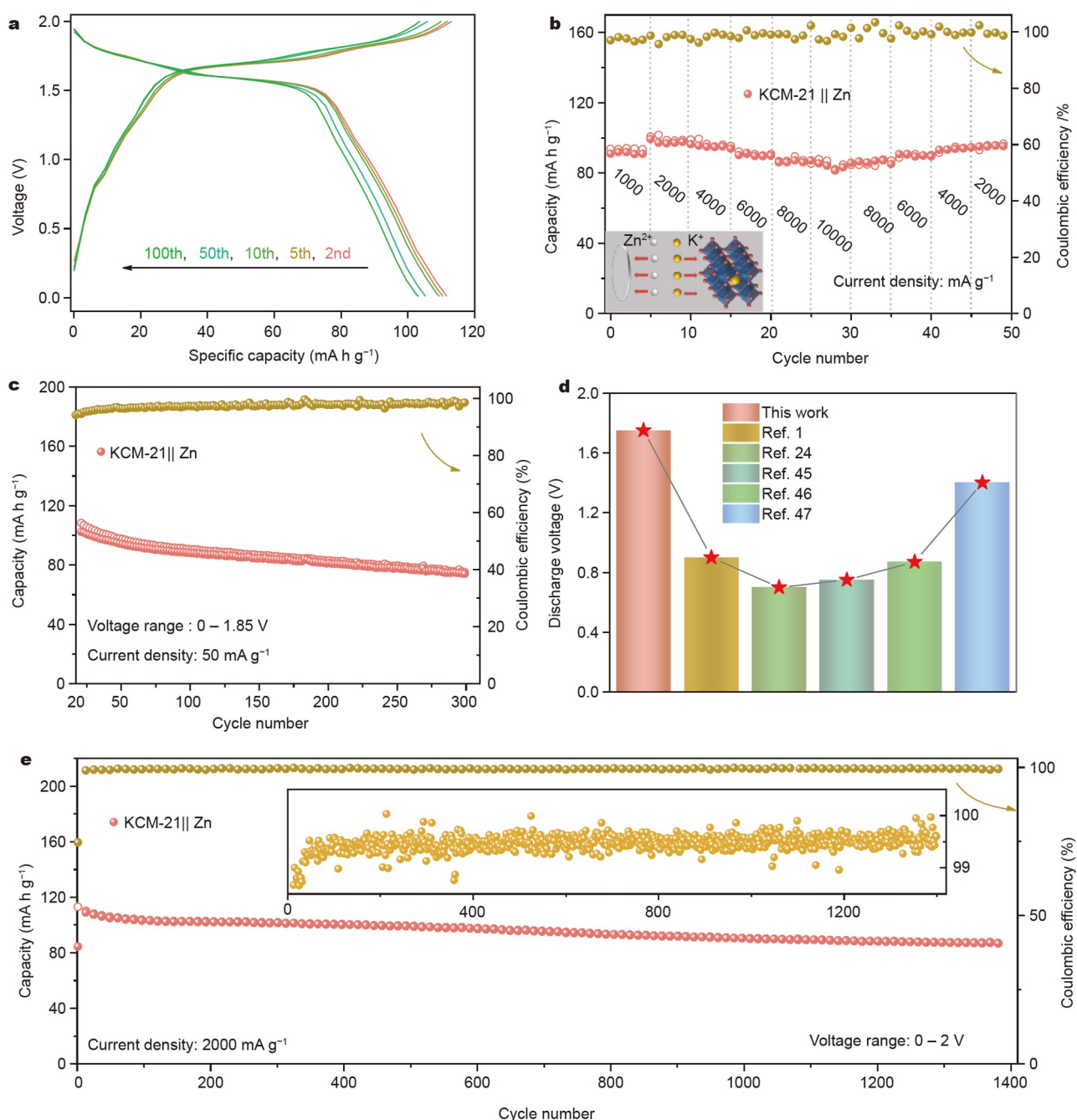
Figure 2 Electrochemical performance of KCM-21||Zn metal batteries. (a) Galvanostatic charge-discharge voltage profiles, (b) rate performance (the inset is a schematic of ion transport mechanism), and (c) cycling performance of PZ-HIB at 50 mA g^{-1}. (d) Comparison of the discharge potential between the reported APBs and PZ-HIB. (e) Long cycle performance of PZ-HIB at the current density of 2000 mA g^{-1}. The inset is the enlarged view of the CE of this battery.

and stripping of Zn^{2+}/Zn on the anode side [42,43]. As shown in Fig. S11b, the CV test was carried out with the scavenging rate of 0.2–1 mV s^{-1}. With the increase in the scavenging rate, the oxidation and reduction peaks shifted to 1.85/1.74 and 1.79/1.61 V, respectively. As the scanning rate increased, the reversibility remained desirable.

Rate performance is a key property during practical applications. Discharge specific capacity was used as the standard. As shown in Fig. 2b, a reversible capacity of 101.7 mA h g^{-1} was provided at 2000 mA g^{-1}. With the continuous increase in the

current density, the reversible capacity showed no evident attenuation. When the current density was increased to 10,000 mA g^{-1}, 83.3% of the original specific capacity was retained; it is the most prominent value reported for APBs thus far [38,44]. On the cathode side, only K$^+$ ions were embedded and released, and on the anode side, Zn^{2+} ions were deposited and dissolved. Ions do not need to shuttle between the electrodes, which greatly shortens their transport path. This property may be the reason for the excellent rate performance of KCM-21||Zn metal batteries (inset, Fig. 2b). To prove this mechanism,

we measured the pristine and discharge states of the KCM-21 powder electrode by EDS elemental mapping (Fig. S12). In the pristine state, K was evenly distributed, and Zn appeared in a light spot because of noise. In the discharge state, the number of K light spots increased, and that of Zn appeared due to noise and partial electrolyte residue. The element proportion was negligible, which indicated that Zn was not embedded into the positive electrode layer during the discharge process. The ionic conductivity of the electrolyte also determined the rate performance of the full battery. We tested the ionic conductivity of the dual-ion electrolyte and obtained a high value of 55.6 mS cm^{-1}, which was due to the high concentration of salt in the electrolyte. The energy storage mechanism of K-Zn dual-ion and high ionic conductivity jointly improved the rate performance of the K-based full battery. When the current density returned to 2000 mA g^{-1}, the specific capacity recovered to 96.7 mA h g^{-1}, and the cycle was stable throughout the whole rate capability test, indicating that the structure of KCM was strong enough to survive high currents. Fig. S13 provides the corresponding charge/discharge curves under different current densities in the rate test. As the current increased, the voltage polarization remained stable, indicating the excellent rate performance of the PZ-HIB.

Fig. 2c shows the cycling performance of PZ-HIB at the current density of 50 mA g^{-1}. KCM-21 can provide a reversible discharge capacity of 103.4 mA h g^{-1} in the 20th cycle. The CE was 95%, and it gradually increased in subsequent cycles, eventually stabilizing at 98.5%. The first 20 cycles were voltage window adjustment processes (Fig. S14). Fig. 2e shows the cycle performance of PZ-HIB at the current density of 2000 mA g^{-1}, and its initial discharge capacity was approximately 111.7 mA h g^{-1} with an ICE of 74.7%. After the first cycle, the CE gradually increased and stabilized at ~99.5% within 20 cycles. The inset in Fig. 2e shows the detailed CE information during the whole cycle. The average value was 99.5%, verifying the high potassiation-depotassiation efficiency at the cathode side and high deposition-stripping efficiency at the anode. After 1400 cycles, the reversible capacity remained at 86.67 mA h g^{-1} (i.e., with a capacity retention of 77.6%). As shown in Fig. S15, KCM-21 had a stable discharge potential of approximately 1.6 V (vs. Zn^{2+}/Zn), showing its highly stable crystal structure. The specific energy of KCM-21 can reach up to 153.74 W h kg^{-1} (calculated based on the second cycle). As the cycle number increased, the charge-transfer resistance gradually decreased (Fig. S16). The initial charge-transfer resistance (R_{ct}) of the as-assembled KCM-21 electrode was 533.31 Ω, but this value gradually decreased to 44.07 Ω after 100 cycles. The resistance of R_{ct} decreased gradually from the initial charge-discharge process, indicating that the enhancement of charge-transfer kinetics gradually increased during the cycling behavior. In summary, by combining the high-voltage KCM-21 cathode and the hybrid-ion mechanism [36], the working voltage of APBs has been significantly improved compared with the reported values (Fig. 2d) [1,24,45–47].

To determine the effect of the Cu-substitution strategy on the electrochemical performance of PBAs, we adjusted the molar ratios of Cu^{2+} and Mn^{2+} to 1:1 and 1:2 under the same synthesis condition of KCM-21 to obtain KCM-11 and KCM-12, respectively. The as-synthesized samples were also applied to the HIB to compare their electrochemical performances with KCM-21. As presented in Fig. S17a, KCM-12 showed the highest initial

capacity of 123.4 mA h g^{-1}, and the values for KCM-11 and KCM-21 were 121.95 and 113.1 mA h g^{-1}, respectively. Therefore, Cu^{2+} did not provide any redox activity in the cathode, which is in line with our predictions. In the subsequent 1000 cycles, KCM-21 showed the most stable cycling performance, maintaining a capacity of 90.8 mA h g^{-1} after 1000 cycles.

In comparison, the capacity of KCM-11 suddenly decreased after 500 cycles, and at the 1000th cycle, it provided a capacity of 50.1 mA h g^{-1}. KCM-12 failed to survive after 220 cycles. In conclusion, with the increase in the Cu^{2+} ratio, although a part of the capacity was sacrificed, better stability can be obtained. Based on the comparison of the 2nd and 200th charge/discharge curves, we analyzed the reason for the capacity attenuation (Fig. S17b, c). The voltage plateau corresponding to Mn^{2+}/Mn^{3+} and Fe^{2+}/Fe^{3+} can be observed in the 2nd cycle of KCM-11 and KCM-12. However, after 200 cycles, the capacity related to the redox of Mn^{2+}/Mn^{3+} decreased sharply for KCM-11 and KCM-12, and the voltage plateau located at 0.87 V was extended, contributing to the decrease in their average discharge voltage. This phenomenon was caused by the dissolution of Mn^{2+} [23,34]. However, this problem was not observed in the KCM-21 sample, confirming the effect of Cu^{2+} on stabilizing the crystal structure of PBAs.

In-situ electrostatic shielding inhibits dendrite growth

Electrostatic shielding is an effective way to inhibit the dendrite growth, and it was often achieved by additional additives in previous studies. In this work, potassium ions in the electrolyte not only ensured the ion contact of cathode and electrolyte but also inhibited the dendrite growth on the anode side.

As shown in Fig. 3a, the rough surface of the zinc foil was a source of dendrites. In the absence of additives, a locally enhanced electric field generated at the tip strongly attracted Zn^{2+}, and dendrites were eventually formed, resulting in the short circuit of batteries. In this work, K^{+} played an important role in the electrolyte. The high oxidation-reduction potential of K^{+} itself did not participate in the anode deposit stripping. Instead, it anchored the tip of a locally enhanced electric field. Zinc ions under the lateral electrostatic interaction moved to the adjacent plane substrate to deposit, thus inhibiting the action of the dendrites. Under constant current conditions, the electrostatic shielding effect of the HIE in Zn‖Zn symmetric batteries was evaluated, and the stability and reversibility of the Zn anode were observed. As shown in Fig. 3e, 2 mol L^{-1} Zn[OTf]$_2$ aqueous electrolytes with the same Zn^{2+} concentration was used for the comparison test. As shown in the black curve, the initial polarization voltage was 94.1 mV, voltage fluctuation occurred at 75 h, and the battery failed at 90 h. The red curve represents the dual-cation electrolyte in this work, showing long-term stability at a current density of 1 mA cm^{-2} without potential fluctuations or short circuits, and the polarization voltage was 34 mV. To observe the surface condition of the cycled Zn foil, we disassembled the Zn‖Zn symmetrical battery and used the cycled zinc foil for the SEM test. As shown in Fig. 3b, the initial Zn foil showed a continuous and smooth surface. However, after 50 cycles, rugby-ball-shaped dendrites appeared on the surface of Zn foil, which cycled in a single-cation electrolyte, with a length of about 700 nm. After 100 cycles, these dendrites further grew to more than 2 μm. When using dual-cation electrolyte (Fig. 3f, g), Zn^{2+} deposited on the surface of Zn foil with a diameter of ~20 nm and uniform distribution after 50 cycles,
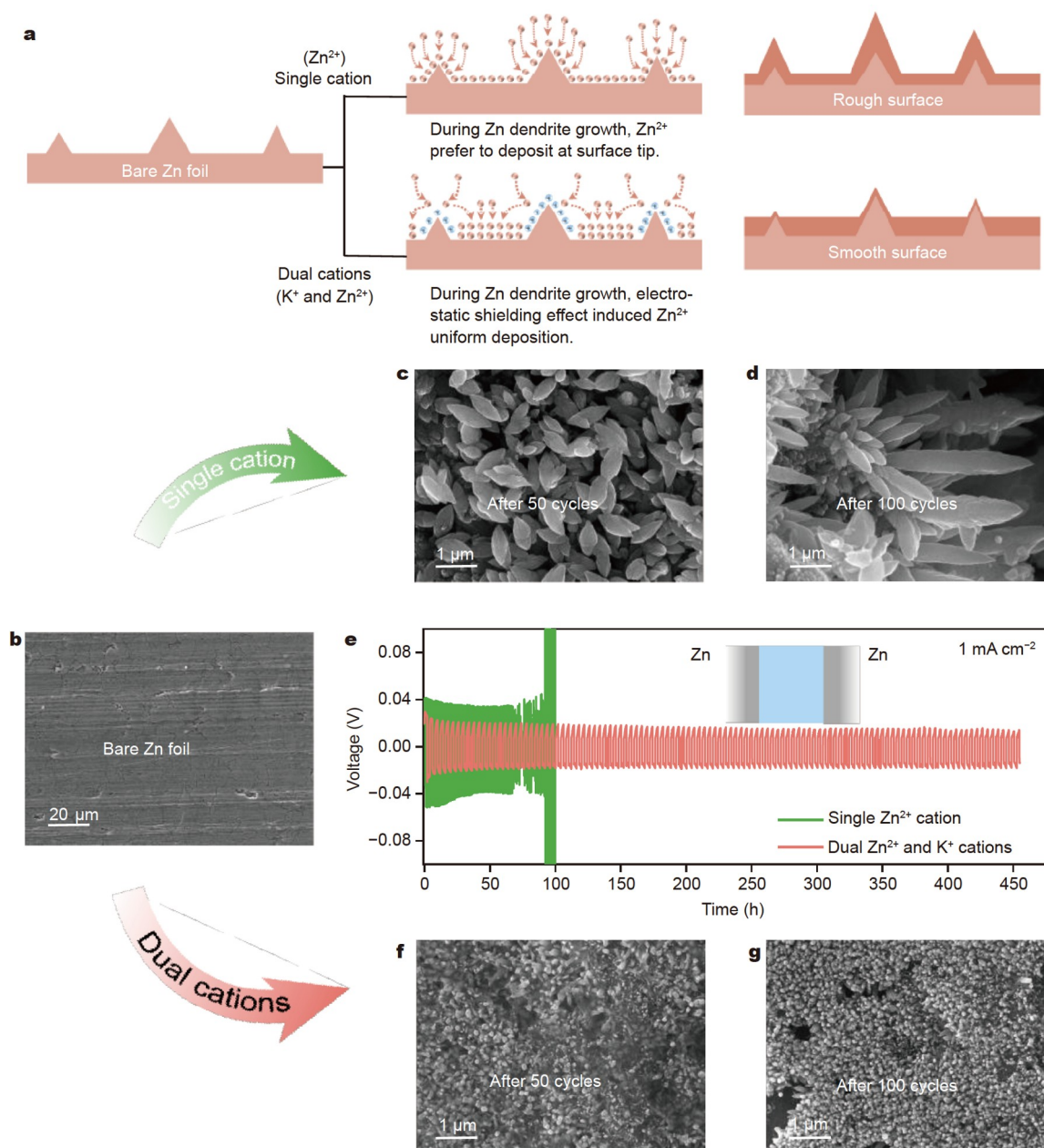
Figure 3 Proof of electrostatic shielding effect. (a) Schematic of dendrite growth inhibition by electrostatic shielding effect. SEM images of the surface of zinc foil (b) before and after cycles in (c, d) single- and (f, g) dual-cation electrolyte. The current density during the cycle was set to 1 mA cm^{-2}. (e) Galvanostatic charge-discharge profiles of Zn||Zn symmetric cells in different electrolytes cycled at the current density of 1 mA cm^{-2}.

and no evident dendrite growth was observed after 100 cycles. With the extension of the cycle process, the point deposition increased, and the diameter increased to ~50 nm. The distribution was uniform, which was acceptable for the mechanical properties of the diaphragm.

To study the electrostatic shielding effect for K$^+$, and we used theoretical kinetic simulations to reveal the zinc ion deposition behavior on the zinc foil with and without K$^+$. Given the source of constant zinc-ion consumption in the electrolyte (simulating zinc deposition under constant current density), we simulated the dynamic balance of Zn^{2+} concentration distribution and calculated the Zn^{2+} distribution through the phase-field method. The electric field was set under the condition that potassium

ions with a high redox potential were priorly anchored at the tip (Fig. S18). The zinc tip was set on the electrode surface, and the point charge of homopolarity was set on the upper part. Fig. 4b, e show the simulation results. The dendrite growth was severe in single-cation electrolytes with a length of 2–3 μm, and the inhibition effect was evident in dual-cation electrolytes. When the concentration field of a single dendrite was locally amplified (Fig. 4a, d), the concentration of zinc ions at the tip was considerably higher than that at the flat end, showing a tip aggregation phenomenon and vertical growth trend of zinc dendrites. In the dual-cation electrolyte, potassium ions were anchored at the top of the dendrite and forced zinc ions to deposit away from the top of the dendrite, relieving the dendrite
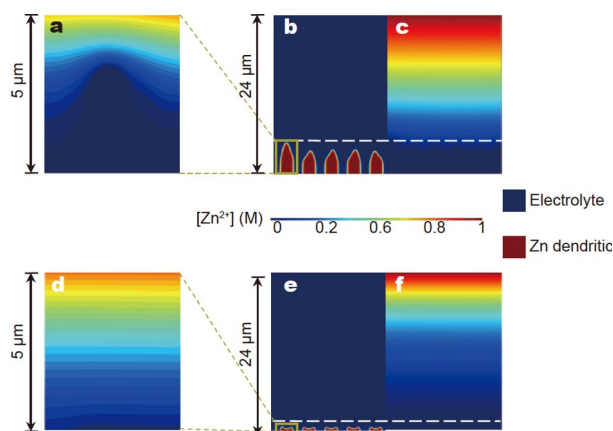
Figure 4 Theoretical kinetic simulation of zinc ion deposition behavior on the anode side. (a, d) Equilibrium Zn-ion concentration profiles with constant-reaction-current electrode surfaces for single and dual cations. (b, e) Initial phase morphologies of the dendrite growth for single and dual cations. (c, f) Zn-ion concentration distribution corresponding to the initial phase morphologies.

growth on the surface of zinc foil. As shown in Fig. 4c, f, the concentration of deposition potential decreased uniformly from the top to bottom. The concentration change in the dendrite tip can be observed in the single-cation system, but it was more hierarchical and uniform in the dual-cation system.

CONCLUSIONS

For the first time, novel APBs were successfully designed and assembled using a dual-cation electrolyte, which has high working potential and excellent rate performance. For the cathode materials, we designed a novel KCM-21 cathode with significantly improved stability by introducing Cu^{2+} to restrain the Jahn-Teller effect. To increase the energy density of APBs, we selected Zn metal as the anode, which has low working potential during the deposition and dissolution process. Based on the new working mechanism from the unique dual-cation electrolyte, the diffusion path of ions in the APB system was greatly shortened, and it greatly improved the rate performance of the full battery. In addition, the electrostatic shielding effect on the negative electrode side formed by the K^+ in this dual-cation electrolyte can effectively inhibit the growth of zinc dendrites. The above study developed a new hybrid-ion mechanism for APBs. This mechanism can be expanded to other AMIBs and contribute to the development of effective strategies to optimize the electrochemical performance of new energy storage systems.

1 Ge J, Fan L, Rao AM, *et al.* Surface-substituted Prussian blue analogue cathode for sustainable potassium-ion batteries. Nat Sustain, 2021, 5: 225–234

2 Luo W, Feng Y, Shen D, *et al.* Engineering ion diffusion by CoS@SnS heterojunction for ultrahigh-rate and stable potassium batteries. ACS Appl Mater Interfaces, 2022, 14: 16379–16385

3 Zhang X, Zhang S, Yang Y, *et al.* A general method for transition metal single atoms anchored on honeycomb-like nitrogen-doped carbon nanosheets. Adv Mater, 2020, 32: 1906905

4 Li Y, Lin S, Wang D, *et al.* Single atom array mimic on ultrathin MOF nanosheets boosts the safety and life of lithium-sulfur batteries. Adv

Mater, 2020, 32: 1906722

5 Yang W, Zhou J, Wang S, *et al.* Freestanding film made by necklace-like N-doped hollow carbon with hierarchical pores for high-performance potassium-ion storage. Energy Environ Sci, 2019, 12: 1605–1612

6 Tang F, Guo S, Sun Y, *et al.* Facile synthesis of Fe-doped CoO nanotubes as high-efficient electrocatalysts for oxygen evolution reaction. Small Struct, 2022, 3: 2100211

7 Piao J, Bin D, Duan S, *et al.* A facile template free synthesis of porous carbon nanospheres with high capacitive performance. Sci China Chem, 2018, 61: 538–544

8 Lei K, Wang C, Liu L, *et al.* A porous network of bismuth used as the anode material for high-energy-density potassium-ion batteries. Angew Chem Int Ed, 2018, 57: 4687–4691

9 Hu Y, Fan L, Rao AM, *et al.* Cyclic-anion salt for high-voltage stable potassium-metal batteries. Natl Sci Rev, 2022, nwac134

10 Yu W, Wang J, Wang Z, *et al.* Pegylation of the antimicrobial peptide PG-1: A link between propensity for nanostructuring and capacity of the antitrypsin hydrolytic ability. J Med Chem, 2021, 64: 10469–10481

11 Ye S, Wang L, Liu F, *et al.* Integration of homogeneous and heterogeneous nucleation growth *via* 3D alloy framework for stable Na/K metal anode. eScience, 2021, 1: 75–82

12 Lei K, Zhu Z, Yin Z, *et al.* Dual interphase layers *in situ* formed on a manganese-based oxide cathode enable stable potassium storage. Chem, 2019, 5: 3220–3231

13 Liu Z, Yang Y, Liang S, *et al.* pH-buffer contained electrolyte for self-adjusted cathode-free Zn-MnO₂ batteries with coexistence of dual mechanisms. Small Struct, 2021, 2: 2100119

14 Zeng X, Xie K, Liu S, *et al.* Bio-inspired design of an *in situ* multifunctional polymeric solid-electrolyte interphase for Zn metal anode cycling at 30 mA cm⁻² and 30 mA h cm⁻². Energy Environ Sci, 2021, 14: 5947–5957

15 Liu S, Mao J, Pang WK, *et al.* Tuning the electrolyte solvation structure to suppress cathode dissolution, water reactivity, and Zn dendrite growth in zinc-ion batteries. Adv Funct Mater, 2021, 31: 2104281

16 Zhang S, Liu Y, Fan Q, *et al.* Liquid metal batteries for future energy storage. Energy Environ Sci, 2021, 14: 4177–4202

17 Qin L, Zhang S, Zheng J, *et al.* Pursuing graphite-based K-ion O₂ batteries: A lesson from Li-ion batteries. Energy Environ Sci, 2020, 13: 3656–3662

18 Cao AM, Hu JS, Wan LJ. Morphology control and shape evolution in 3D hierarchical superstructures. Sci China Chem, 2012, 55: 2249–2256

19 Tan H, Zhou Y, Qiao SZ, *et al.* Metal organic framework (MOF) in aqueous energy devices. Mater Today, 2021, 48: 270–284

20 Yu W, Liu Z, Yu X, *et al.* Balsa-wood-derived binder-free freestanding carbon foam as high-performance potassium anode. Adv Energy Sustain Res, 2021, 2: 2100018

21 Ren X, Zhao Q, McCulloch WD, *et al.* MoS₂ as a long-life host material for potassium ion intercalation. Nano Res, 2017, 10: 1313–1321

22 Lei Y, Han D, Dong J, *et al.* Unveiling the influence of electrode/ electrolyte interface on the capacity fading for typical graphite-based potassium-ion batteries. Energy Storage Mater, 2020, 24: 319–328

23 Jiang L, Lu Y, Zhao C, *et al.* Building aqueous K-ion batteries for energy storage. Nat Energy, 2019, 4: 495–503

24 Su D, McDonagh A, Qiao SZ, *et al.* High-capacity aqueous potassium-ion batteries for large-scale energy storage. Adv Mater, 2017, 29: 1604007

25 Shen D, Rao AM, Zhou J, *et al.* High-potential cathodes with nitrogen active centres for quasi-solid proton-ion batteries. Angew Chem Int Ed, 2022, 61: e202201972

26 Cheng N, Xu P, Lu B, *et al.* Covalent sulfur as stable anode for potassium ion battery. J Energy Chem, 2021, 62: 645–652

27 Li F, Wu S, Li D, *et al.* The water catalysis at oxygen cathodes of lithium-oxygen cells. Nat Commun, 2015, 6: 7843

28 Sun T, Li ZJ, Zhi YF, *et al.* Poly(2,5-dihydroxy-1,4-benzoquinonyl sulfide) as an efficient cathode for high-performance aqueous zinc-organic batteries. Adv Funct Mater, 2021, 31: 2010049

29 Chen S, Kuang Q, Fan HJ. Dual-carbon batteries: Materials and mechanism. Small, 2020, 16: 2002803

30 Wu L, Gu M, Feng Y, *et al.* Layered superconductor Cu₀.₁₁TiSe₂ as a

high-stable K-cathode. Adv Funct Mater, 2022, 32: 2109893

31 Liu Z, Wang J, Lu B. Plum pudding model inspired KVPO$_4$F@3DC as high-voltage and hyperstable cathode for potassium ion batteries. Sci Bull, 2020, 65: 1242–1251

32 You Y, Yao HR, Xin S, et al. Subzero-temperature cathode for a sodium-ion battery. Adv Mater, 2016, 28: 7243–7248

33 Gebert F, Cortie DL, Bouwer JC, et al. Epitaxial nickel ferrocyanide stabilizes Jahn-Teller distortions of manganese ferrocyanide for sodium-ion batteries. Angew Chem Int Ed, 2021, 60: 18519–18526

34 Li WJ, Chou SL, Wang JZ, et al. Multifunctional conducting polymer coated Na$_{1+x}$MnFe(CN)$_6$ cathode for sodium-ion batteries with superior performance via a facile and one-step chemistry approach. Nano Energy, 2015, 13: 200–207

35 Wessells CD, Huggins RA, Cui Y. Copper hexacyanoferrate battery electrodes with long cycle life and high power. Nat Commun, 2011, 2: 550

36 Fan L, Ma R, Wang J, et al. An ultrafast and highly stable potassium-organic battery. Adv Mater, 2018, 30: 1805486

37 Fan X, Gaddam RR, Kumar NA, et al. A hybrid Mg^{2+}/Li$^+$ battery based on interlayer-expanded MoS$_2$/graphene cathode. Adv Energy Mater, 2017, 7: 1700317

38 Zhu Y, Yin J, Zheng X, et al. Concentrated dual-cation electrolyte strategy for aqueous zinc-ion batteries. Energy Environ Sci, 2021, 14: 4463–4473

39 Deng L, Qu J, Niu X, et al. Defect-free potassium manganese hexacyanoferrate cathode material for high-performance potassium-ion batteries. Nat Commun, 2021, 12: 2167

40 Gao C, Liu Y, Zheng L, et al. The effect of electrolyte type on the Li ion intercalation in copper hexacyanoferrate. J Electrochem Soc, 2019, 166: A1732–A1737

41 Bie X, Kubota K, Hosaka T, et al. Synthesis and electrochemical properties of Na-rich Prussian blue analogues containing Mn, Fe, Co, and Fe for Na-ion batteries. J Power Sources, 2018, 378: 322–330

42 Ma X, Cao X, Yao M, et al. Organic-inorganic hybrid cathode with dual energy-storage mechanism for ultrahigh-rate and ultralong-life aqueous zinc-ion batteries. Adv Mater, 2022, 34: 2105452

43 Yu Z, Cao L, Liu H, et al. High voltage aqueous Zn/LiCoO$_2$ hybrid battery under mildly alkaline conditions. Energy Storage Mater, 2021, 43: 158–164

44 Eftekhari A, Jian Z, Ji X. Potassium secondary batteries. ACS Appl Mater Interfaces, 2017, 9: 4404–4419

45 Ling T, Da P, Zheng X, et al. Atomic-level structure engineering of metal oxides for high-rate oxygen intercalation pseudocapacitance. Sci Adv, 2018, 4: eaau6261

46 Wessells CD, Peddada SV, Huggins RA, et al. Nickel hexacyanoferrate nanoparticle electrodes for aqueous sodium and potassium ion batteries. Nano Lett, 2011, 11: 5421–5425

47 Wu XY, Sun MY, Shen YF, et al. Energetic aqueous rechargeable sodium-ion battery based on Na$_2$CuFe(CN)$_6$-NaTi$_2$(PO$_4$)$_3$ intercalation chemistry. ChemSusChem, 2014, 7: 407–411

Author contributions Yu W and Ge J conducted the experiment; Wu L and Luo W did some characterizations. Lu B, Hu Y, Shen D and Chen S performed some data analysis and offered helpful suggestions. Liu Z, Zhou J and Yang H designed this study. All authors contributed to the general discussion.

Conflict of interest The authors declare that they have no conflict of interest.

Supplementary information Supporting data are available in the online version of the paper.

Weijian Yu received his BSc and master degrees in electronic science and technology from Hunan University (HNU) in 2019. He is currently a doctoral candidate at Harbin Institute of Technology (HIT). His research interests focus on the modification of electrolytes for Li/Na/Zn-ion batteries.

Junmin Ge received his doctorate degree from the Department of Physics and Electronics, HNU in 2021. He is currently a researcher at Zhengzhou University. His research interests focus on noval high-safety energy storage batteries.

Bingan Lu is a professor and doctoral supervisor at HNU. Prof. Lu's research mainly focuses on the research of new energy storage materials and devices including Li/K/Al-ion batteries. He is on the Editorial Board or Youth Editorial Board of National Science Review, Molecules, Science China Technological Sciences, InfoMat, and SmartMat.

混合体系: 一种改善水系钾离子全电池能量密度和稳定性的有效方式

于伟健[1†], 盖军民[1†], 胡艳瑶[1], 沈东阳[1], 罗文迪[1], 陈素华[2], 武利琛[1], 刘朝孟[3], 周江[4], 杨红官[1*], 鲁兵安[1,5*]

摘要 水系钾基电池(APBs)因具有高安全性和环境友好的性质而被广泛研究. 然而, 由于电极材料和工作机制的限制, APBs在倍率性能和能量密度方面需要进一步提高, 以满足发展需求. 针对上述问题, 我们首次成功设计并组装了以Zn金属作为阳极, K$_{1.92}$Cu$_{0.62}$Mn$_{0.38}$-[Fe(CN)$_6$]$_{0.968}$·□$_{0.032}$·H$_2$O$_{0.35}$作为阴极, 2 mol L^{-1} Zn(SO$_3$CF$_3$)$_2$ + 12 mol L^{-1} KSO$_3$CF$_3$作为电解液的水系钾基电池. 这种混合离子体系的设计优点是: (i) 选择金属锌作为阳极, 提高了APBs的工作电位; (ii) 双阳离子储存机制缩短了离子传输路径; (iii) 来自双阳离子电解质的K$^+$通过静电屏蔽作用抑制了锌枝晶的生长. 因此, 组装后的全电池具有1.75 V的高工作电位, 并具有优异的倍率性能(在10,000 mA g^{-1}的电流密度下, 保持原有容量的83.3%). 此外, 通过理论相场模拟和综合表征充分揭示了原位静电屏蔽效应, 显著抑制了锌阳极的枝晶生长, 提高了全电池稳定性. 混合离子电池的结构设计为高性能APBs的发展提供了思路.